Structural Evolution of Ag-LEV Zeolite upon Heating: An In Situ Single-Crystal X-ray Diffraction (SC-XRD) and X-ray Absorption Spectroscopy (XAS) Study

Georgia Cametti, Andreas C. Scheinost, Sergey, V Churakov

ACS OMEGA

http://pubs.acs.org/journal/acsodf

Article

Structural Evolution of Ag-LEV Zeolite upon Heating: An In Situ Single-Crystal X-ray Diffraction (SC-XRD) and X-ray Absorption Spectroscopy (XAS) Study

Georgia Cametti,* Andreas C. Scheinost, and Sergey V. Churakov

Cite This: *ACS Omega* 2020, 5, 31774−31783

Read Online

ACCESS | Metrics & More | Article Recommendations | Supporting Information

ABSTRACT: Ag-exchanged zeolites are known to have improved sorption and catalytic properties compared to the raw natural material. The application range of Ag-exchanged zeolites is linked to the stability of the exchanged form and its structural evolution at high temperatures. In this study, we investigated the thermal stability of a Ag-exchanged zeolite with an **LEV** framework type. The dehydration path was monitored in situ by single-crystal X-ray diffraction (SC-XRD) and X-ray absorption fine structure spectroscopy (XAFS). The experimental data were compared with those extrapolated from molecular dynamics (MD) trajectories. Our results showed that Ag-exchanged levyne (Ag-LEV) follows a different dehydration path compared to that of the natural levyne (Ca-LEV). Between 25 and 350 °C, the unit cell volume contraction was −4% with respect to that measured at room temperature. Upon dehydration, Ag-LEV transformed to the LEV B topology: such transformation is accompanied by the change from $R\bar{3}m$ to $R3m$ space group and by the onset of the rupture of one T−O−T connection at 250 °C. Differently from Ca-LEV, no additional change to LEV B′ configuration was detected. XAFS analysis indicated that each Ag is approximately surrounded by four oxygen atoms between 2.15 and 2.40 Å. This local environment was maintained up to 650 °C. Weak Ag^{+1}−Ag^{+1} interactions, detected in the whole investigated temperature range, are mainly ascribed to the presence of Ag-erionite (Ag-ERI) intergrown with Ag-LEV. No reduction to elemental Ag^0 occurred upon heating.

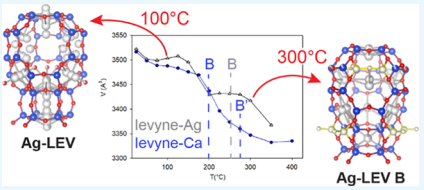

1. INTRODUCTION

Microporous zeolites have a well-defined framework structure and exchangeable extraframework (EF) cations. This property is often used to incorporate selected cations capable of improving their performance in a diverse range of applications. In particular, Ag-modified zeolites have received great attention because of their improved catalytic, photocatalytic, sorption, and antibacterial properties.[1−5] Regardless of their structure and chemical composition, zeolites usually undergo modifications upon heating, which include change of the pores size, diffusion of the extraframework species, and collapse of the three-dimensional structure.[6,7] Further, zeolites with the same framework topology can respond differently to the heating stimuli depending on the nature of the EF cations in the structural pores.[8−10] With respect to Ag species incorporated in the zeolite voids, they can experience, at high temperatures (HT), a change in the oxidation state, leading to the formation of Ag clusters.[1,2] These modifications have an impact on the zeolite properties, directly influencing their use. Thus, the study of the temperature-induced transformations is extremely important to optimize and tune subsequent applications. In the case of Ag-exchanged zeolites, the following aspects have been proved to play a key role: (i) the position of silver atoms with respect to the tetrahedral framework, (ii) the nature of Ag species within the zeolitic pores, and (iii) the structural evolution (of both framework and extraframework) occurring upon dehydration.

Zeolites with **LEV** framework type are particularly interesting because their structure combines small pore openings with a large micropore volume (0.3 cm^3/g).[11] For this reason, the **LEV** framework type is considered as one of the most relevant among the small-pore zeolites with eight-membered ring opening, and diverse synthesis routes have been developed.[12] The rhombohedral **LEV** framework type is described by a sequence of single six-membered rings (6mR) and double six-membered rings (D6R) stacked along the c-axis in an AABCCABBCAA sequence.[13] This stacking creates alternating [$4^9 6^5 8^3$] (*lev* cage) and [$4^6 6^2$] polyhedra (D6R) along [001]. Two systems of interconnected eight-membered ring channels run parallel to [001].

The thermal stability of **LEV** topology was studied on natural crystals of levyne-Ca with ideal chemical composition $NaCa_{2.5}(Al_6Si_{12}O_{36})\cdot 18H_2O$.[14,15] Upon heating, levyne-Ca undergoes severe structural modifications as a consequence of dehydration, involving the statistical rupture of the T−O−T bonds of the framework.[16,17] Temperature-resolved synchrotron X-ray powder diffraction data (XRPD) reported a

Received: September 11, 2020
Accepted: October 22, 2020
Published: December 3, 2020

Table 1. Crystal Data and Refinement Parameters of Ag-LEV at 50, 100, 125, 150, 225, 250, and 300 °C

crystal data	Ag-LEV 50	Ag-LEV 100	Ag-LEV 125	Ag-LEV 150
a (Å)	13.3661(4)	13.2511(19)	13.2131(3)	13.1150(4)
c (Å)	22.6328(8)	23.039(5)	23.2393(10)	23.4675(13)
V (Å^3)	3501.7(2)	3503.5(12)	3513.7(2)	3495.7(3)
Z	3	3	3	3
space group	$R\bar{3}m$	$R\bar{3}m$	$R3m$	$R3m$
refined chemical formula	$Ag_{3.43}(Si,Al)_{18}O_{36}{\cdot}10.3H_2O$	$Ag_{3.0}(Si,Al)_{18}O_{36}{\cdot}3.3H_2O$	$Ag_{4.61}(Si,Al)_{18}O_{36}{\cdot}4.4H_2O$	$Ag_{3.80}(Si,Al)_{18}O_{36}{\cdot}1.4H_2O$
crystal size (mm)	0.180 × 0.150 × 0.150	0.180 × 0.150 × 0.150	0.180 × 0.150 × 0.150	0.180 × 0.150 × 0.150
intensity measurement				
diffractometer	APEX II SMART	APEX II SMART	APEX II SMART	APEX II SMART
X-ray radiation	Mo Kα λ = 0.71073 Å	Mo Kα λ = 0.71073 Å	Mo Kα λ = 0.71073 Å	Mo Kα λ = 0.71073 Å
X-ray power	50 kV, 30 mA	50 kV, 30 mA	50 kV, 30 mA	50 kV, 30 mA
monochromator	graphite	graphite	graphite	graphite
temperature (°C)	50	100	125	150
time per frame (s)	10	10	10	10
max. 2θ (deg)	54.61	54.27	53.20	49.77
index ranges	$-13 \le h \le 17$	$-12 \le h \le 16$	$-12 \le h \le 16$	$-12 \le h \le 15$
	$-17 \le k \le 16$	$-16 \le k \le 16$	$-16 \le k \le 16$	$-15 \le k \le 15$
	$-29 \le l \le 20$	$-29 \le l \le 21$	$-22 \le l \le 29$	$-27 \le l \le 22$
no. of measured reflections	11 930	12 357	11 545	10 958
no. of unique reflections	988	974	1690	1441
no. of observed reflections $I > 2\sigma(I)$	873	833	1398	1236
structure refinement				
no. of parameters used in the refinement	96	96	162	139
R (int)	0.0403	0.0446	0.0398	0.0528
R (σ)	0.0212	0.0212	0.0294	0.0360
GooF	1.033	1.129	1.113	1.101
R_1, $I > 2\sigma(I)$	0.0597	0.0778	0.0723	0.0862
R_1, all data	0.0660	0.0856	0.0850	0.0946
w$R2$ (on F^2)	0.1805	0.2395	0.2143	0.2491
$\Delta\rho_{min}$ (eÅ^{-3}) close to	−0.98 Ag1	−0.71 O1	−1.28 Ag4B	−1.14 Ag1C
$\Delta\rho_{max}$ (eÅ^{-3}) close to	1.05 W1A	1.03 Ag5A	0.89 Ag4A	0.91 Ag44
BASF	0.052(5)	0.045(8)	0.050(11)	0.063(16)

crystal data	Ag-LEV 225	Ag-LEV 250	Ag-LEV 300
a (Å)	12.9559(18)	12.955(3)	12.912(3)
c (Å)	23.611(5)	23.623(5)	23.670(5)
V (Å^3)	3432.3(12)	3433.5(17)	3417.4(17)
Z	3	3	3
space group	$R3m$	$R3m$	$R3m$
refined chemical formula	$Ag_{3.18}(Si,Al)_{18}O_{36.2}$	$Ag_{3.0}(Si,Al)_{18}O_{36}$	$Ag_{2.6}(Si,Al)_{18}O_{36}$
crystal size (mm)	0.180 × 0.150 × 0.150	0.180 × 0.150 × 0.150	0.180 × 0.150 × 0.150
intensity measurement			
diffractometer	APEX II SMART	APEX II SMART	APEX II SMART
X-ray radiation	Mo Kα λ = 0.71073 Å	Mo Kα λ = 0.71073 Å	Mo Kα λ = 0.71073 Å
X-ray power	50 kV, 30 mA	50 kV, 30 mA	50 kV, 30 mA
monochromator	graphite	graphite	graphite
temperature (°C)	225	250	300
time per frame (s)	10	10	10
max. 2θ (deg)	54.96	53.94	40.16
index ranges	$-11 \le h \le 16$	$-16 \le h \le 16$	$-12 \le h \le 11$
	$-15 \le k \le 12$	$-12 \le k \le 16$	$-10 \le k \le 12$
	$-30 \le l \le 22$	$-22 \le l \le 30$	$-21 \le l \le 22$
no. of measured reflections	7557	12 120	6941
no. of unique reflections	1713	1717	833
no. of observed reflections $I > 2\sigma(I)$	874	1049	654
structure refinement			
no. of parameters used in the refinement	127	99	91
R (int)	0.0633	0.0761	0.0751
R (σ)	0.0783	0.0537	0.0485
GooF	0.908	1.089	1.102
R_1, $I > 2\sigma(I)$	0.0645	0.0758	0.0874

https://dx.doi.org/10.1021/acsomega.0c04455
ACS Omega 2020, 5, 31774−31783

Table 1. continued

crystal data	Ag-LEV 225	Ag-LEV 250	Ag-LEV 300
R_1, all data	0.1254	0.1198	0.1102
w$R2$ (on F^2)	0.1967	0.2416	0.2522
$\Delta\rho_{min}$ (eÅ^{-3}) close to	−0.81 Ag5	−0.79 Ag4	−0.63 O11
$\Delta\rho_{max}$ (eÅ^{-3}) close to	0.60 Ag5	0.77 T11B	0.73 Ag2A
BASF	0.091(8)	0.095(10)	0.09(2)

transformation above 230 °C to a new topology, levyne B, with stacking sequence ABCBCACAB.[16] This structure is characterized by a system of edge-sharing tetrahedra that are mutually exclusive. Since the rupture of the framework connections is a statistical process, the anhydrous levyne comprises a mixture of the original **LEV** and the new LEV B topologies. The dehydration behavior of levyne-Ca was also investigated by in situ single-crystal X-ray diffraction (SC-XRD).[17] The structural changes observed in this case upon heating were different compared to those reported by the XRPD experiments. First of all, the transformations occurring upon dehydration took place at lower temperatures; second, an additional T−O−T connection broke at 275 °C, leading to the formation of a new levyne B topology, called levyne B′. The latter is still characterized by an uninterrupted framework, but it can adopt diverse topologies depending on which of the new tetrahedral sites are occupied. The conclusion was that even if the average symmetry $R\bar{3}m$ is maintained at a high temperature, individual topologies might have lower symmetry.

Recently, we reported the room-temperature structure of Ag-exchanged levyne (Ag-LEV) in space group $R\bar{3}m$.[18] Silver ions were found to be strongly disordered at partially occupied sites (occupancy lower than 0.32) distributed along the threefold axis and, differently from levyne-Ca (Ca-LEV), at the wall of the eight-membered ring window of the *lev* cage. In the same study, we could perform a chemical and structural characterization of an erionite fragment (another zeolite belonging to the ABC 6 family[15]) intergrown with levyne. We could demonstrate that: (i) erionite was also modified during the exchange experiment and (ii) Ag ions occupy the *eri* cavity, whereas K^+ in the cancrinite cage was not replaced.

The aim of the present study was to determine the influence of Ag uptake on levyne thermal stability. For this purpose, we tracked for the first time the in situ dehydration behavior of Ag-LEV using two complementary techniques: accurate information on the structural transformations were obtained by single-crystal X-ray diffraction (SC-XRD), whereas X-ray absorption fine structure spectroscopy (XAFS) was used to provide an insight into the local environment of Ag ions inside the zeolitic cages and to establish the eventual formation of Ag clusters. The experimental results were then compared and corroborated by theoretical calculations from ab initio molecular dynamics (MD) simulations.

2. METHODS

2.1. Sample Description. The sample under investigation was the Ag-LEV produced in our previous study.[18] This specimen consisted of levyne intergrown with erionite.[18] For the single-crystal X-ray experiments, a single fragment of Ag-levyne (chemical composition $Ag_{6.1}Al_{6.3}Si_{11.8}O_{36}\cdot 18.0H_2O$[18]) could be selected, and, consequently, the erionite had no influence on the obtained results. In contrast, XAFS measurements were performed on the powdered sample (see Section 2.3) that included erionite fragments as well. The levyne/erionite ratio in the pristine material was 54:46, as estimated by semi-quantitative X-ray powder diffraction analysis (S1).

2.2. Single-Crystal X-ray Diffraction (SC-XRD). The single-crystal used for X-ray diffraction experiments was the same used and characterized at room temperature (RT) in our previous study.[18] Diffraction data were collected using a Bruker Apex II diffractometer equipped with Mo Kα radiation (0.71073 Å) and a CCD detector. The dehydration process was investigated from 50 to 300 °C in steps of 25 °C and from 300 to 350 °C in steps of 50 °C, using the same experimental apparatus described in ref 17. Each data collection lasted for ca. 7 h. The crystal was equilibrated at the set temperature for at least 40 min before starting a new data collection. Such experimental conditions can be regarded as dry and quasi-equilibrium conditions.

Data were integrated and corrected for absorption by using the software package APEX3 v2019.1-0.[19] Two methods were employed to solve the structures: (i) direct methods, using ShelXTL[20] after determining the space group by Xprep,[19] and (ii) intrinsic phasing, using ShelxT.[21] The first approach indicated $R\bar{3}m$ space group for datasets up to 100 °C. From 125 °C on, the suggested space group, based on R_{sym} and figure of merit, was $R\bar{3}$. The results obtained by the intrinsic phasing method mainly suggested $R3m$, $R\bar{3}m$, and $R32$ for all datasets. However, the correct space group could not be unequivocally assigned because of the close values of the indicators R_{weak}, α, and x (initial Flack's parameter determined for noncentrosymmetric space groups).[21] Thus, we performed a series of structural refinements in the centric ($R\bar{3}m$, $R\bar{3}$) and noncentric ($R3$, $R3m$, $R32$) solutions. Finally, the acentric space group $R3m$ was chosen for all datasets from 125 to 300 °C, based on the R_1 values and weighting scheme of the structural refinements. The centrosymmetric space groups $R\bar{3}m$ and $R\bar{3}$ (and the acentric $R32$) were excluded based on the arrangement of the extraframework (EF) occupants and subsequent change of the framework observed at high temperatures (see the Section 3).

Structural refinements were carried out by SHELXL-2014[22] using neutral atomic scattering factors. Atom labels and coordinates of framework atoms were those used by Cametti and Churakov, 2020.[18] Extraframework species were located by difference Fourier maps. Atomic sites related by a pseudo-center of symmetry in $R3m$ were labeled by doubling the number of digits of the corresponding site in $R\bar{3}m$. For instance, in $R\bar{3}m$, two independent tetrahedral sites T1 and T2 constitute the framework. In $R3m$, the two independent tetrahedral sites equivalent to T1 were labeled as T1 and T11. Reverse-obverse twinning [$\bar{1}00$ $0\bar{1}0$ 001] was observed for all structures in the investigated temperature range.

The dataset collected at 200 °C was affected by high R_{int} values, and a reasonable structure solution and refinement was not possible. With the increase of temperature, the intensity of the reflections significantly decreased. At 275 and 300 °C the maximum theta value was 45.39° (resolution = 0.94 Å) and

https://dx.doi.org/10.1021/acsomega.0c04455
ACS Omega 2020, 5, 31774−31783

40.16° (resolution = 1.0 Å), respectively. Thus, for these two datasets, structure refinements, although with a poor data/parameter ratio (Table 1), were possible. At 350 °C, only cell parameters were extracted. Crystal data, data collection, and refinement details are reported in Table 1. All visualizations of crystal structures were produced by VESTA.[23] Cif files are available in the Supporting Information.

2.3. X-ray Absorption Fine Structure Spectroscopy (XAFS). XAFS experiments were performed at the European Synchrotron Radiation Facility (ESRF) in Grenoble, France. The data were collected at the Spanish CRG beamline (SPLINE, BM25) equipped with a Rh-coated collimating mirror, a sagitally focusing Si(111) double-crystal monochromator, and a Rh-coated vertically focusing mirror. The sample was gently ground, and the resulting powder was inserted in a 0.7 mm glass capillary. Spectra were collected at the Ag K-edge (25 514 eV) in transmission mode using gas-filled ionization chambers. The high temperature (HT) measurements were performed in situ by using a N_2 blower (FMB Oxford). Data were recorded from 25 to 650 °C at the following temperatures: 25, 75, 175, 275, 350, 425, 550, and 650 °C. The equilibration time between each data collection was 10 min.

Each scan was recorded up to k = 12.0 Å^{-1} with a typical acquisition time of 30 min. To improve the signal-to-noise ratio, five scans were averaged at each temperature.

XAFS data were reduced using WinXAS software.[24] For each spectrum, the background was subtracted, and the absorption edge jump was normalized to unity. The energy was then converted to photoelectrons kinetic energy (k-space) by assigning the ionization energy of the Ag K-edge to the first inflection point of the absorption edge. To perform EXAFS analyses, k^3-weighted $\chi(k)$ were Fourier-transformed between 2.0 and 9.2 Å^{-1} using a Kaiser−Bessel window function. The spectra were fitted using the WinXAS software[24] as well. The scattering paths were calculated by FEFF 8.2[25,26] based on the structure of Ag-levyne.[18] The amplitude reduction factor (S_0^2) was fixed to 0.9. For all scattering paths, a global phase shift ΔE_0 was fitted and the Debye−Waller factor was constrained from 0.001 to 0.01 Å^2. The evolution of EXAFS spectra as a function of temperature was analyzed by principal component analysis (PCA)[27] and iterative target transformation factor analysis (ITFA) using the software package ITFA.[28,29]

2.3.1. Calculations of Theoretical XAFS Spectra. Theoretical $\chi(k)$ functions were calculated based on the atomic configuration from ab initio molecular dynamic simulations of Ag-LEV performed in our previous study (model of Ag-levyne with $2H_2O$).[18] The calculations were extended to 30 ps and the data were collected from a 16 ps long MD trajectory followed by 14 ps equilibration time. This trajectory represents the equilibrium thermal motion of atoms in the structure at RT conditions. The details of the simulation and the modeling parameters are provided in Supporting Information Section S2.

Theoretical extended X-ray absorption fine structure (EXAFS) spectra were obtained using 130 consecutive MD snapshots separated by 125 fs interval. EXAFS spectra for each Ag scattering atom in the supercell were calculated using FEFF 8.40 software.[24,25] In total 34 × 130 spectra were averaged to obtain a reference ab initio EXAFS spectrum per MD trajectory. The Fermi energies and the scattering potential were calculated self-consistently using the cluster radius of 4.0 Å. Multi-scattering paths up to four legs with path lengths up to 8.0 Å were taken into account. Since the structural disorder is accounted for in MD trajectories, the Debye−Waller factor was set to a low value of 0.0002 Å^2. The amplitude reduction factor (S_0^2) was set to 0.9. A similar protocol was recently used for the EXAFS spectra of structural Fe in clay minerals[30,31] and heavy metals in zeolites.[32,33]

In addition, to take into account the erionite intergrowths present in the powder used for EXAFS experiments, theoretical $\chi(k)$ functions were calculated for the Ag-erionite structure. The structural model was taken from experimental diffraction data[18] using a unit cell containing 12 Ag, 3K, 15 Al, 39 Si, 136 O, and 56 H. EXAFS spectra were calculated for each Ag position in the unit cell using FEFF 8.40 software.[25,26]

3. RESULTS AND DISCUSSION

3.1. Structural Modifications upon Heating. All structural refinements failed to locate all Ag ions per unit cell predicted by the chemical composition.[18] A lack of approximately 25% of Ag apfu was already reported[18] for the structure of Ag-LEV measured at RT. This lack was justified because of the strong disorder of EF cations. Thus, it is not surprising that with an increase temperature and a further decrease of reflection intensity, the amount of missing Ag became even more pronounced (refined chemical composition in Table 1).

The unit cell volume trend as a function of temperature is reported in Figure 1. In the investigated temperature range, the total contraction is approximately −4% with respect to the unit cell volume measured at RT. This contraction is accompanied by gradual release of water, migration of the EF cations, and final rupture of T−O−T framework connections. The relevant structural changes occurring upon heating are reported below.

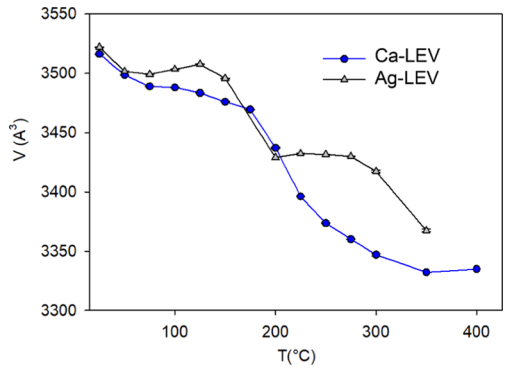

Figure 1. Evolution of the unit cell volume of Ag-LEV (gray triangles) as a function of temperature. The corresponding trend of Ca-LEV[17] (blue circles) is shown for comparison. Adapted with permission from "Cametti, G.; Churakov, S. V. Crystal structure of Ag-exchanged levyne intergrown with erionite: single-crystal X-ray diffraction and molecular dynamics simulations. *Am. Mineral.* **2020**, DOI: https://doi.org/10.2138/am-2020-7500". Copyright 2020 Mineralogical Society of America.

The dehydration of Ag-LEV starts at 50 °C, when the structure releases part of the H_2O at the W3 site, the occupancy of which decreases from 0.485(15) at RT[18] to 0.279(16) (Table S1). Simultaneously, silver ions at Ag4 sites (Ag4A...Ag4E) slightly rearrange their position. In particular, Ag4B and Ag4E come closer (1.14(7) Å) to the W3 site. Such a short distance must be interpreted considering a mixture of H_2O and Ag ions at these positions.

https://dx.doi.org/10.1021/acsomega.0c04455
ACS Omega 2020, 5, 31774−31783

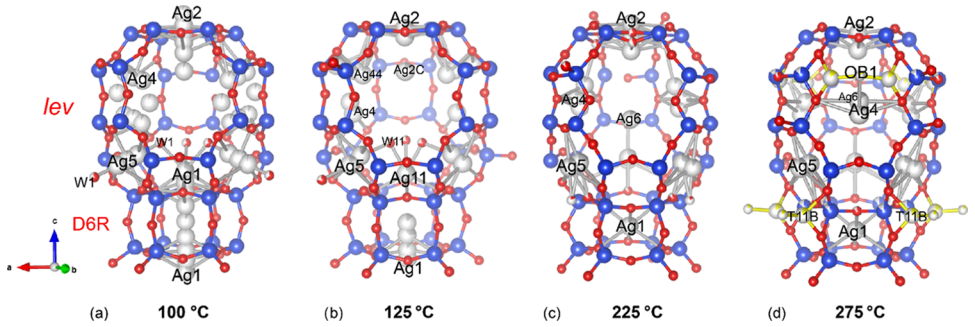

Figure 2. *Lev* cavity and D6R cage of Ag-LEV crystal structures measured at 100 (a), 125 (b), 225 (c), and 275 °C (d). The blue and red spheres represent Si and O atoms, respectively. Ag atoms are displayed in gray. Partial occupancy of crystallographic sites is shown by partially colored spheres. The new tetrahedral sites, originating as a consequence of the T−O−T rupture, are reported in yellow.

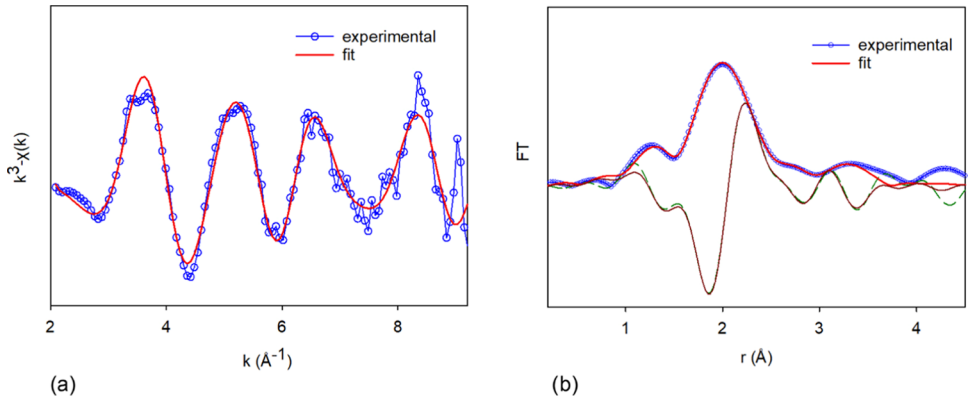

Figure 3. (a) $k^3\chi(k)$ weighted and (b) Fourier transform EXAFS spectra (uncorrected for phase shift) of Ag-LEV sample intergrown with Ag-ERI at 25 °C. Experimental data and corresponding fit are reported as blue circles and continuous lines, respectively. Measured (dashed line) and fitted (continuous line) imaginary parts of FT are also displayed.

At 100 °C, H_2O at W3 is completely released and the W1 occupancy decreases to 0.60(3) (Table S2). The release of water is accompanied by the rearrangement of the EF cations: the Ag1 site shifts towards the center of the D6R cage, at (000), as indicated by the appearance of three additional low-occupied sites (Ag1B, Ag1C, Ag1D) distributed along the threefold axis in correspondence of the (000) position (Figure 2a and Table S2). Ag4D and AgE disappear, and new electron density peaks appear in the middle of the 6mR lateral window of the *lev* cavity. Such residual electron density was modeled by two sites (Ag5 and Ag5A) between two H_2O at W1 sites in two adjacent channels (Figure 2a). Although Ag scattering factors were used to refine Ag5 and Ag5A sites, it is more likely that at this temperature, these positions are occupied by a mixture of H_2O and silver ions.

At 125 °C, the structure was refined in the acentric space group *R*3*m*. The acentricity of the space group became evident from the distribution of Ag ions. The Ag1 site approaches the center of the D6R cage (Figure 2b). Silver mainly concentrates at Ag1 (occ. 0.233(19)) and Ag1D (occ. 0.22(4)) sites (Table S3). However, part of it remains outside the D6R, at Ag11 (occ. = 0.325(17)) (Figure 2b). The occupancy of W1 and W11 (that are symmetry-equivalent in $R\bar{3}m$) converges to approximately the same value, but H_2O at W11 symmetry-equivalent positions become closer to each other (Figure 2b), most probably to facilitate the bonding with Ag5A. Silver at Ag2 forms three longer bonds with oxygen atoms at O5 (2.70 Å) and three shorter with those at O55 (2.47 Å). Silver in the eight-membered ring window dispersed in the upper (Ag44, Ag4B, and Ag4C) and middle (Ag4 and Ag4A) parts of it.

With the increase of temperature, the migration of the EF cations continues, and at 150° C H_2O at W11 is completely released whereas the occupancy of W1 decreases to 0.53(12) (Table S4). At this temperature, most of the silver originally at the Ag1 position is in the D6R cage in octahedral coordination with oxygen atoms of the framework. The Ag11 site retains 15% Ag, which is still bonded to the remaining H_2O at W1. Simultaneously, Ag4 sites migrate toward the center of the eight-membered ring window, whereas the occupancies of Ag5 and Ag5A increase to 0.273(12) and 0.107(13), respectively.

The diffraction data collected at 200 °C were affected by high R_{int} and R_{sigma}, and a tentative structural refinement was not satisfactory. It is worth noting that this temperature corresponds to the decrease of the unit cell volume (Figure 1). At 225 °C, the structure is anhydrous. Ag1 occupies 50% of the D6R cages, and Ag4, Ag4A, and AgB relocate approximately in the center of the eight-membered ring window, and an additional low-occupied Ag site (Ag6) appeared in the center of the *lev* cavity (Figure 2c and Table S5).

At 250 °C, a tiny peak ($0.52e^-/Å^3$) was observed at 1.70 and 1.95 Å from O4 and T11, respectively. This peak was refined with Si scattering factors and represents a new tetrahedral site (T11B) occurring because of the onset of the T11−O22−T11 breaking process (Table S6). The latter becomes more obvious with increasing temperature (Figure 2d and Table S7): at 300 °C the new apices OB1 and OB2 were located and the new

https://dx.doi.org/10.1021/acsomega.0c04455
ACS Omega 2020, 5, 31774−31783

Table 2. Structural Parameters of Ag-LEV Intergrown with Ag-ERI at 25, 275, 350, and 650 °C Determined from EXAFS Data[a,b,c,d]

	EXAFS											
	25 °C			275 °C			350 °C			650 °C		
shell	CN ±25%	R (Å) ±0.02	σ^2 (Å^2) ±0.002	CN ±25%	R (Å) ±0.02	σ^2 (Å^2) ±0.002	CN ±25%	R (Å) ±0.02	σ^2 (Å^2) ±0.002	CN ±25%	R (Å) ±0.02	σ^2 (Å^2) ±0.002
Ag−O_1	1.21	2.15	0.01	0.90	2.10	0.005	1.32	2.19	0.01	1.38	2.14	0.009
Ag−O_2	2.20	2.40	0.005	3.42	2.36	0.01	1.64	2.41	0.002	1.69	2.38	0.003
Ag−O_3	1.14	2.94	0.001	1.34	2.92	0.001	0.93	2.93	0.001	0.85	2.88	0.001
Ag−Ag	1.04	3.28	0.01	1.21	3.27	0.01	0.93	3.30	0.01	0.77	3.26	0.01
Ag−Si	0.78	3.41	0.001	0.87	3.39	0.001	0.80	3.41	0.004	1.37	3.36	0.01
ΔE_0(eV)	1.11			0.09			1.57			−1.00		
χ-residual	2.80			2.28			4.28			4.14		

[a]The uncertainty for each parameter is reported. [b]CN: coordination number. [c]R: Absorber−scatterer distance. [d]σ^2: Debye−Waller factor.

T11B tetrahedra formed. Final occupancies of T11B converged to 0.25 (Table S8).

3.2. Local Configuration of Ag^{+1}. The $k^3\chi(k)$ weighted EXAFS and the corresponding Fourier transform (FT) best fits of the sample measured at 25 °C are reported in Figure 3. The FT EXAFS spectrum (uncorrected for phase shift) indicates no long-range order for Ag atoms in the levyne structure, in agreement with diffraction data at RT.[18] The best fit is obtained considering five shells: three Ag−O, one Ag−Ag, and one Ag−Si (Table 2). The first two peaks of the FT magnitude (FTM) at ca. 1.3 and 2.0 Å (distance uncorrected for phase shift) can be attributed to two Ag−O shells, indicating approximately one oxygen at 2.15 Å (Ag−O_1 shell) and 2.2 oxygen atoms at 2.40 Å (Ag−O_2 shell) (Table 2). An additional Ag−O shell (Ag−O_3) suggested the occurrence of one more oxygen at a longer distance (2.94 Å). The FTM peak in the 3−4 Å FTM region was fitted by Ag−Si and Ag−Ag shells. The presence of a heavy backscatterer in this region was evidenced by a wavelet plot peak extending into the >9 Å^{-1} k-region.[34] Note that the fitted Ag−Ag distance of 3.28 Å is much longer than that expected for elemental silver (2.89 Å).

The EXAFS-derived distances for Ag−O_2, Ag−O_3, and Ag−Si shells are in good agreement with those reported by XRD and MD simulations. An exiguous contribution of Ag−Ag distances is also present in the modeled structure (only 0.15 silver atoms are found at 3.25 Å from each Ag) (Figure S1). The shortest Ag−O distance reported by XRD data was 2.25(4) Å for Ag4C-W3 sites.[18] An inspection of the Ag−O contacts calculated from MD trajectories pointed out that approximately 0.20 oxygen atoms of the H_2O are found at 2.15−2.20 Å to Ag, whereas no significant contribution can be observed for framework oxygen atoms (Figure S1).

The interpretation of the spectroscopic results cannot be exclusively based on the Ag-LEV structure but must consider the occurrence of intergrown erionite as well. Indeed, differently from the SC-XRD measurements, where a single fragment of levyne was used, the sample in XAFS experiments consisted of a powder, where both mineral phases were present (see Section 2.1). As demonstrated in our previous study,[18] erionite is also affected by ion exchange and consequently contributes to the XAFS signal. As a confirmation of this, discrepancies, particularly evident in the range between 6 and 9 Å^{-1}, are observed if the experimental $k^3\chi(k)$ function is compared with that calculated from MD trajectories of Ag-LEV (Figure S2). The aforementioned range corresponds to a heavy backscatterer contribution, the presence of which is also confirmed by the EXAFS-fitting.

To ascertain the influence of Ag-erionite on the measured $\chi(k)$ function, different structural configurations based on XRD data[18] were tested. In general, the theoretical spectra calculated for Ag-ERI better reproduce the peaks between 6 and 9 Å^{-1} of the experimental $k^3\chi(k)$ weighted EXAFS. The $\chi(k)$ function of the Ag-ERI structure, which better represents the experimental data, is reported in Figure S3. Finally, the best match was obtained considering a mixture of 50:50 of calculated Ag-LEV and Ag-ERI spectra (Figure 4). Based on

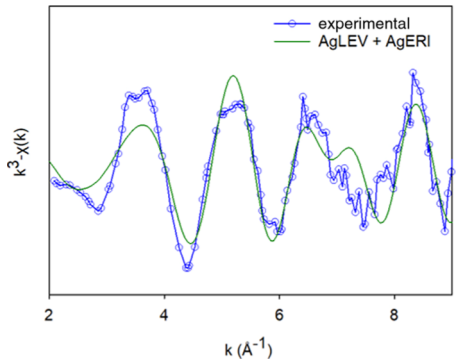

Figure 4. Computed $k^3\chi(k)$-weighted function (green line) hypothesizing a 50:50 mixture of Ag-LEV (model from MD trajectories) and Ag-ERI (model from XRD data[18]). The blue circles represent experimental data at 25 °C.

the model retrieved from X-ray data[18] (Figure S4), in Ag-ERI, local Ag−O configuration is comparable to that in Ag-LEV, whereas Ag−Ag contacts are more significant. Ag−Ag distances between 3.2 and 3.3 Å are found between C1 and C3 sites refined by XRD data.[18]

3.2.1. Evolution of Ag Local Environment upon Heating. The experimental EXAFS spectra as a function of temperature are reported in Figure 5. Although all measured spectra could be nicely reproduced with only one component, abstract concentration distribution suggests a continuous change with temperature. Assuming two components, the VARIMAX rotation (Figure S5) shows three different temperature stages: stage 1, from 25 to 75° C, stage 2 from 175 to 350 °C, and stage 3 from 425 to 650 °C. Since they are described with two principal components, there are only two different local structures, the first one prevailing in stage 1 and the second one prevailing in stage 3. The local structure in stage 2 is a mixture of those in stages 1 and 3. In spite of this, fit parameters along the HT series vary only slightly (though

https://dx.doi.org/10.1021/acsomega.0c04455
ACS Omega 2020, 5, 31774−31783

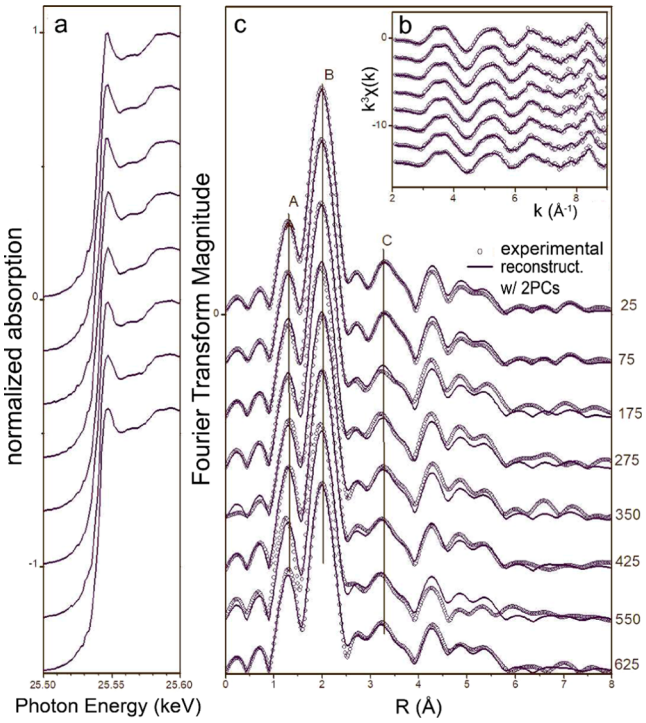

Figure 5. Evolution of XANES (a), $k^3\chi(k)$-weighted EXAFS spectra (b), and corresponding FT (c) of Ag-LEV sample intergrown with Ag-ERI as a function of temperature. Experimental data and reconstruction by two components calculated by ITFA (b, c) are represented by circles and lines, respectively. The lines A, B, and C are a guide to the eye for the evolution of the three main peaks as a function of temperature.

significantly) (Table 2), meaning that upon dehydration, silver rearranges its position to maintain a coordination very similar to the one adopted at RT.

The five-shell model could successfully fit EXAFS data at high temperatures. The structural parameters obtained at 275 °C (Table 2) can be compared with those extrapolated by XRD at the same temperature. According to X-ray analysis, the structure at this temperature is supposed to be anhydrous; hence, all Ag−O interactions refer to framework oxygen atoms. In general, the distances estimated by the two techniques are in good agreement: EXAFS-refined short Ag−O contacts (2.10 Å), attributed to Ag-H_2O at RT, can be associated with bond length between Ag and the new oxygen apex OB1 (Ag4−OB1 = 2.14(10) Å). Also, the Ag−O interactions at 2.36 Å are comparable to Ag1−O22 (2.45(3) Å), Ag2−O5 (2.37(3) Å), and Ag2B−O5 (2.34(3) Å) bond lengths. In contrast, according to X-ray structural refinements, due to cation rearrangement, Ag−Ag distances of 3.3 Å are no longer observed. Thus, such distances are ascribed to Ag ions in erionite.

3.3. Dehydration and "Acentricity" of the Structure. The main structural modifications occurring upon heating can be summarized as (i) the shrinking of the unit cell volume, with a total volume contraction of 4% and (ii) partial breaking of T−O−T linkages observed for T11−O22−T11 and T11−O33−T11. These changes are driven by the rearrangement and migration of the EF cations. In particular, upon dehydration:

- Ag1 migrates along the threefold axis to reach the D6R cage.
- Ag2 mainly remains in the middle of the 6mR window at the top of *lev* cavity.
- Ag4 rearranges its position and relocates in the middle of the 8mR aperture of the *lev* cavity.
- Additional silver progressively moves toward the 6mR lateral window of *lev* cavity at the Ag5 site, which is finally 20% occupied.

As suggested by EXAFS data, this relocation allows Ag ions to maintain a very similar coordination to that stable at RT.

In the light of our results, the structure of Ag-LEV is pseudocentrosymmetric, i.e., the framework topology is centrosymmetric, whereas the heavy atom substructure is noncentrosymmetric. The latter becomes evident only upon dehydration. Thus, the change from $R\bar{3}m$ to $R3m$ should be interpreted as a gradual process, driven by the rearrangement of the EF cations upon heating. Two main observations justify the acentric configuration:

- First, the different release of H_2O from pseudosymmetry-equivalent sites (W1 and W11) at 150 °C.
- Second, the T−O−T breaking between 250 and 300 °C, which was obvious for the T11 but not for its pseudosymmetry-related site T1.

The rupture of the T−O−T connections is a statistical process which involves, at 300 °C, approximately 20% of the tetrahedral T11 sites. This means that at this temperature the two topologies, **LEV** and LEV B, coexist. The presence of a mixture of two different structural configurations is also confirmed by PCA of EXAFS spectra. In this case, however, the occurrence of the erionite phase does not allow an unequivocal interpretation. Moreover, no clear structural differences can be observed between the local Ag environment at 25 and 650 °C (Table 2). Nevertheless, the gradual and slight change upon heating in XAFS spectra correlates with that demonstrated by XRD analysis. We can speculate that the first two temperature stages recognized by VARIMAX rotation (Figure S5), are roughly related to the unit cell volume trend determined by XRD (Figure 1). From 25 to 150 °C, a gradual volume decrease is observed and the structure is supposed to retain some water molecules; this first step could be associated with the one from 25 to 75 °C in Figure S5 (note that no XAFS spectra between 75 and 175 °C were collected). The temperature range between 200 and 350 °C, at which the structure is assumed to be anhydrous, would correspond to the second stage (from 175 to 350 °C). In this temperature interval, two structural configurations are supposed to coexist, but they cannot be directly identified with **LEV** and LEV B topologies, since the T−O−T breaking was detected by XRD only at 275 °C. Most probably, such mismatch is related to the presence of Ag-erionite. Therefore, even if evolution as a function of temperature is also recognized in the EXAFS spectra, the role of Ag-erionite in such change remains unclear.

3.4. Differences to Ca-LEV. If the EF cations replacement with Ag has not an explicit influence on the structure at RT,[18] it does affect the framework behavior upon heating. The topology of the dehydrated structure, assuming only T1, T11B, and T2 tetrahedra, forms the ABCBCACAB stacking sequence (Figure 6), which corresponds to that of levyne B, observed for levyne-Ca at 230 °C by XRPD[16] and between 200 and 275 °C by SC-XRD.[17]

To have an unbiased comparison between the natural form and the Ag-exchanged one, we must compare our results with those obtained by Cametti, 2018[17] using the same specimen

https://dx.doi.org/10.1021/acsomega.0c04455
ACS Omega 2020, 5, 31774−31783

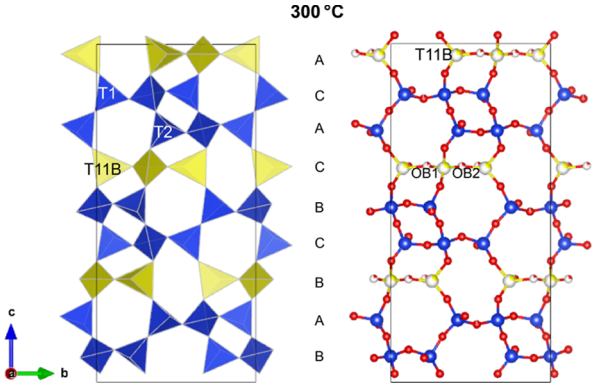

Figure 6. Polyhedral and ball-stick representation of the crystal structure of Ag-LEV B at 300 °C. New tetrahedral sites forming as a consequence of the T−O−T rupture are depicted in yellow. The stacking sequence ABCBCACAB of the 6mR along c is also reported.

and, most importantly, the very same experimental setup. Based on this result, the dehydration path of Ag-levyne is clearly different from that of the pristine material. Although both processes follow a similar trend up to 200 °C, from this temperature, the unit cell volume of Ag-LEV remains almost steady up to 300 °C, when its value is 2% larger than that measured for Ca-LEV (Figure 1).

In natural Ca-LEV, two T−O−T ruptures were detected at 200 and 275 °C, respectively. Both processes were associated with the release of water and subsequent migration of EF cations toward new positions. In Ag-LEV, the breaking process involving the T11−O22−T11 linkages occurs at 250 °C, when the occupancy of the T11 site decreased to 0.941(9) and the new tetrahedral site T1B appeared. Considering the occupancies of the new T sites, the process is significantly less pronounced compared to that observed in natural Ca-LEV, for which at 225 °C the occupancy of T1B reached already 0.142(3).[17]

The release of water could not be unambiguously monitored because of the strong disorder of Ag ions and H_2O. However, we can identify the complete dehydration in correspondence of the drop of the unit cell volume at 200 °C. This would also agree with the fact that no additional tetrahedral bond breaking is observed in the investigated T range, compared to the pristine material, meaning that no residual water is retained beyond 200 °C. This becomes clearer by looking at the unit cell volume trend in Figure 1. Between RT and 200 °C, the volume contraction of Ag-LEV follows a similar trend to that of natural levyne. From 200 °C on, the unit cell of Ca-LEV further shrinks, but not that of Ag-LEV, indicating that, in this case, the structure is most probably anhydrous.

The fact that in Ag-LEV there is no water left after the first dehydration step also agrees with the conclusions we drew based on the characterization of RT structure. In our previous study,[18] the H_2O content at RT was estimated based on molecular dynamics simulations. The best agreement with experimental data was obtained for the Ag-LEV structure containing 2 H_2O per formula unit, in contrast to 3 H_2O found in natural levyne-Ca.[15] Thus, the lack of a second dehydration step, associated with the rupture of the second T−O−T connection observed in Ca-LEV, is explained by less water content in Ag-LEV at RT.

3.5. Ag^+ Speciation within the Pores. The formation of Ag clusters inside zeolite cavities is of particular interest because of their role in sorption and photocatalytic properties.[1,2,4] Different kinds of clusters (neutral, charged, and partially charged $Ag_n^{\delta+}$) have been reported in many zeolite structures,[1,35−38] as a function of the degree of Ag-exchanged, thermal treatment, or reducing atmosphere.[39−42] Due to disorder and partial occupancy of EF sites, the occurrence of Ag clusters in our sample cannot be clearly investigated by SC-XRD. In this specific case, we rely on MD simulations and EXAFS analysis.

In our sample, Ag−Ag interactions at 3.25 Å are mainly assigned to the intergrown Ag-ERI phase. Similar distances were reported for Ag−X[39] and Ag−A,[43] where some silver reduction occurred. However, in our case, the presence of elemental silver is not validated by XANES spectra (Figure 5a). Furthermore, Ag−O distances are too short (between 2.14 and 2.45 Å) to be ascribed to Ag^0−O. We conclude that weak Ag^+−Ag^+ interactions[39] and, as a consequence the formation of Ag^+−Ag^+ clusters, are likely to occur in Ag-ERI but not in Ag-LEV.

The reduction of Ag^{+1} into Ag^0 has been reported for many Ag-exchanged zeolites under different treatment conditions. Different factors have been proved to influence the reduction process, such as the reaction time,[41] the presence of flow oxygen during dehydration,[39] the Al content of the framework,[35] and in general, the structure of the zeolite host.[36] For example, Hutson and co-workers,[2] observed no Ag reduction in Ag-exchanged zeolite Y dehydrated in vacuum for 4 h. Similarly, in a Ag-exchanged zeolite X, dehydrated under oxygen flow at 360 °C and evacuated at 400 °C at 2×10^{-6} Torr for 2 h, no neutral Ag was observed.[39] In contrast, Ag neutral clusters were observed in a Ag-zeolite-X structure by prolonging the evacuation time to 2 days.[41]

Thus, the lack of Ag^0 formation in our sample could be either due to the dehydration method we applied or related to framework topology. Interestingly, another Ag-zeolite with **STI** framework type, dehydrated under the very same conditions we applied in the present study,[32] also showed no Ag reduction.

4. CONCLUSIONS

The effect of EF cations on the thermal stability of natural zeolites and, as a consequence, on the phase transformations occurring as a function of dehydration is a well-established phenomenon.

In Ag-exchanged zeolites, the electronic state and structural position of Ag species (cationic Ag^+, reduced Ag^0, or partially charged $Ag_n^{\delta+}$ clusters) are key factors controlling their functionality. For instance, Ag^0 and Ag^+ have antimicrobial properties,[44] partially charged $Ag_n^{\delta+}$ clusters have photoluminescence properties[1] and are active for NO_x selective catalytic reaction (SCR).[45,46] Dispersed cationic Ag^+ was found to be active for both NO_xSCR[46] and photocatalytic decomposition of NO.[46,47]

In this study, we could ascertain the effect of Ag incorporation on levyne thermal stability combining the information gained from two experimental techniques coupled with theoretical computations. In conclusion, the main difference in the dehydration behavior of Ag-LEV compared to Ca-LEV is the lack of transformation to the levyne B′ phase. Concerning Ag ions in the **LEV** framework type, the following conclusions can be drawn: (i) as a function of temperature, Ag ions migrate within the cavities to maintain a favorable coordination that is found to be very similar to that of the RT

https://dx.doi.org/10.1021/acsomega.0c04455
ACS Omega 2020, 5, 31774−31783

structure; (ii) the Ag−O bonds (from 2.14 to 2.4 Å) are characteristic of short covalent bonds, in agreement with the low coordination number of silver; (iii) weak Ag^{1+}−Ag^{1+} distances occur in Ag-LEV only at RT, whereas they persist in the intergrown Ag-ERI phase up to 650 °C.

The practical usefulness, applicability, and efficiency of zeolites in industrial processes and laboratory tests are controlled by the stability of the specific framework structures under different environmental conditions. The structural modifications via ion exchange can, at various extents, lead to change of the microporous framework and extend or narrow the stability field of such a framework. In our study, for the first time, the dehydration behavior of Ag-LEV was revealed in situ using complementary techniques. The study shows that the thermal-induced phase transformations of the structural network in Ag-LEV as a function of temperature and water content are different from the behavior of the pristine material. This finding is particularly interesting when taking into consideration the fact that Ag-LEV experiences a smaller contraction of the channels. Notably, this is not always the case, as demonstrated, for example, for **STI** framework-type materials, where Ag incorporation lead to a more pronounced volume contraction upon dehydration.[32] Furthermore, the study was able to clearly rule out the potential presence of extraframework Ag in the metallic form. This was only possible by combined use of spectroscopic studies and quantum mechanical calculations. Due to numerous factors that can influence Ag^0 formation within zeolite cavities, our results can contribute to shed light on the role of such factors in the eventual Ag reduction.

■ ASSOCIATED CONTENT

Supporting Information

The Supporting Information is available free of charge at https://pubs.acs.org/doi/10.1021/acsomega.0c04455.

Powder diffraction analysis of the pristine material; details on molecular dynamics simulations; atom coordinates, atomic displacement parameters, and occupancy of Ag-LEV structure at 50, 100, 125, 150, 225, 250, 275, and 300 °C; running coordination number of Ag−O and Ag−Ag contacts in Ag-LEV structure; experimental $k^3\chi(k)$ weighted $\chi(k)$ function of Ag-LEV sample compared with calculated $k^3\chi(k)$ weighted $\chi(k)$ of Ag-LEV; calculated $k^3\chi(k)$ weighted $\chi(k)$ of Ag-ERI; structural model of Ag-ERI; and Varimax rotation of the HT series EXAFS spectra assuming two components (PDF)

Crystallographic data of Ag-LEV RT (CIF)

Crystallographic data of Ag-LEV 100 °C (CIF)

Crystallographic data of Ag-LEV 125 °C (CIF)

Crystallographic data of Ag-LEV 150 °C (CIF)

Crystallographic data of Ag-LEV 225 °C (CIF)

Crystallographic data of Ag-LEV 250 °C (CIF)

Crystallographic data of Ag-LEV 275 °C (CIF)

Crystallographic data of Ag-LEV 300 °C (CIF)

■ AUTHOR INFORMATION

Corresponding Author

Georgia Cametti − *Institute of Geological Sciences, 3012 Bern, Switzerland;* orcid.org/0000-0002-3186-3074; Email: georgia.cametti@geo.unibe.ch

Authors

Andreas C. Scheinost − *The Rossendorf Beamline at the European Synchrotron Radiation Facility (ESRF), 38043 Grenoble, France; Institute of Resource Ecology, 01328 Dresden, Germany;* orcid.org/0000-0002-6608-5428

Sergey V. Churakov − *Institute of Geological Sciences, 3012 Bern, Switzerland; Paul Scherrer Institut, 5232 Villigen PSI, Switzerland;* orcid.org/0000-0001-8213-9206

Complete contact information is available at: https://pubs.acs.org/10.1021/acsomega.0c04455

Author Contributions

G.C. conceived the research, performed the experiments, analyzed the data, and wrote the manuscript. A.C.S. analyzed the XAFS data. S.V.C. supervised and set up the MD simulations. The manuscript was written through contributions of all authors. All authors have given approval to the final version of the manuscript.

Funding

This study benefits from funding awarded to G.C. by the Swiss National Science Foundation (SNF): Ambizione Grant No. PZOOP2_173997.

Notes

The authors declare no competing financial interest.

■ ACKNOWLEDGMENTS

The authors are thankful to Dr. Beda Hoffman of Natural History Museum of Bern who provided the levyne sample. The authors acknowledge access to the Swiss National Supercomputing Centre (CSCS) and UBELIX HPC cluster at University of Bern. They also thank Germán Castro of the Spanish CRG Beamline at ESRF in Grenoble for his support and help during the XAFS experiments and Thomas Armbruster for reading and commenting the paper.

■ REFERENCES

(1) Coutino-Gonzalez, E.; Baekelant, W.; Grandjean, D.; Roeffaers, M. B. J.; Fron, E.; Aghakhani, M. S.; Bovet, N.; Van der Auweraer, M.; Lievens, P.; Vosch, T.; et al. Thermally activated LTA(Li)-Ag zeolites with water-responsive photoluminescence properties. *J. Mater. Chem. C* **2015**, *3*, 11857−11867.

(2) Hutson, N. D.; Reisner, B. A.; Yang, R. T.; Toby, B. H. Silver ion-exchanged zeolites Y, X, and low-silica X: Observations of thermally induced cation/cluster migration and the resulting effects on the equilibrium adsorption of Nitrogen. *Chem. Mater.* **2000**, *12*, 3020−3031.

(3) Ferreira, L.; Fonseca, A. M.; Botelho, G.; Aguiar, C. A.; Neces, I. C. Antimicrobial activity of faujasite zeolites doped with silver. *Microporous Mesoporous Mater.* **2012**, *160*, 126−132.

(4) Aghakhani, S.; Grandjean, D.; Baekelant, W.; Coutiño-Gonzales, E.; Fron, E.; Kvashnina, K.; Roeffaers, M. B. J.; Hofkens, J.; Sels, B. F.; Lievens, P. Atomic scale reversible opto-structural switching of few atom luminescent silver clusters confined in LTA zeolites. *Nanoscale* **2018**, *10*, 11467−11476.

(5) Milenkovic, J.; Hrenovic, J.; Matijasevic, D.; Niksic, M.; Rajic, N. Bactericidal activity of Cu-, Zn-, Ag-containing zeolites toward *Escherichia coli* isoltates. *Environ. Sci. Pollut. Res.* **2017**, *24*, 20273−20281.

(6) Cruciani, G. Zeolites upon heating: Factors governing their thermal stability and structural changes. *J. Phys. Chem. Solids* **2006**, *67*, 1973−1994.

(7) Alberti, A.; Martucci, A. Reconstructuve phase transitions in microporous materials: Rules and factors affecting them. *Microporous Meosporous Mater.* **2011**, *141*, 192−198.

(8) Sun, H.; Wu, D.; Guo, X.; Navrotsky, A. Energetics and structural evolution of Na-Ca exchanged zeolite A during heating. *Phys. Chem. Chem. Phys.* **2015**, *17*, 9241−9247.
(9) Lee, Y.; Seoung, D.; Liu, D.; Park, M. B.; Hong, S. B.; Chen, H.; Bai, J.; Kao, C.; Vogt, T.; Lee, Y. In situ dehydration studies of fully K-, Rb-, and Cs-exchanged natrolites. *Am. Mineral.* **2011**, *96*, 393−401.
(10) Wu, L.; Navrotsky, A. Synthesis and thermodynamic study of transition metal ion (Mn^{2+},Co^{2+},Cu^{2+}, and Zn^{2+}) exchanged zeolites A and Y. *Phys. Chem. Chem. Phys.* **2016**, 10116−10122.
(11) Yamamoto, K.; Ikeda, T.; Onodera, M.; Muramatsu, A.; Mizukami, F.; Wang, Y.; Gies, H. Synthesis and structure analysis of RUB-50, an LEV-type aluminosilicate zeolite. *Microporous Mesoporous Mater.* **2010**, *128*, 150−157.
(12) Dusselier, M.; Davis, M. E. Small-Pore zeolites: synthesis and catalysis. *Chem. Rev.* **2018**, *118*, 5265−5329.
(13) Barrer, R. M.; Kerr, I. S. Intracrystalline channels in levynite and some related zeolites. *Trans. Faraday Soc.* **1959**, *55*, 1915−1923.
(14) Merlino, S.; Galli, E.; Alberti, A. The crystal structure of levyne. *TMPM, Tschermaks Mineral. Petrogr. Mitt.* **1975**, *22*, 117−129.
(15) Gottardi, G.; Galli, E. *Natural Zeolites*; Springer-Verlag: Berlin, Heidelberg, New York, Tokyo, 1985.
(16) Arletti, R.; Vezzalini, G.; Quartieri, S.; Cámara, F.; Alvaro, M. A new framework topology in the dehydrated form of zeolite levyne. *Am. Mineral.* **2013**, *98*, 2063−2074.
(17) Cametti, G. New topology of levyne B under quasi-equilibrium conditions: a temperature dependent single crystal X-ray diffraction study. *Microporous Mesoporous Mater.* **2018**, *265*, 162−171.
(18) Cametti, G.; Churakov, S. V. Crystal structure of Ag-exchanged levyne intergrown with erionite: single crystal X-ray diffraction and molecular dynamics simulations. *Am. Mineral.* **2020**, No. 7500.
(19) *Bruker AXS*, APEX3 v2019.1-0, 2019.
(20) Sheldrick, G. M. A short history of SHELX. *Acta Crystallogr., Sect. A: Found. Adv.* **2008**, *64*, 112−122.
(21) Sheldrick, G. M. SHELXT- Integrated space-group and crystal structure determination. *Acta Crystallogr., Sect. A: Found. Adv.* **2014**, *71*, 3−8.
(22) Scheldrick, G. M. Crystal structure refinement with SHELXL. *Acta Crystallogr., Sect. C: Struct. Chem.* **2015**, *71*, 3−8.
(23) Momma, K.; Izumi, F. VESTA 3 for three-dimensional visualization of crystal, volumetric and morphology data. *J. Appl. Crystallogr.* **2011**, *44*, 1272−1276.
(24) Ressler, T. WinXAS: A Program for X-ray absorption spectroscopy data analysis under MS-Windows. *J. Synchrotron Radiat.* **1998**, *5*, 118−122.
(25) Ankudinov, A. L.; Ravel, B.; Rehr, J. J.; Conradson, S. D. Real-space multiple-scattering calculation and interpretation of X-Ray-absorption near-edge structure. *Phys. Rev. B* **1998**, *58*, 7565−7576.
(26) Ankudinov, A. L.; Rehr, J. J. Theory of solid-state contributions to the X-Ray elastic scattering amplitude. *Phys. Rev. B* **2000**, *62*, 2437−2445.
(27) Abdi, H.; Williams, L. J. Principal component analysis. *Comput. Stat.* **2010**, *2*, 433−459.
(28) Malinowski, E. R.; Howery, D. G. *Factor Analysis in Chemistry*; Wiley Interscience: New York, 1980.
(29) Rossberg, A.; Reich, T.; Bernhard, G. Complexation of uranium(VI) with protocatechuic acid - application of iterative transformation factor analysis to EXAFS spectroscopy. *Anal. Bioanal. Chem.* **2003**, *376*, 631−638.
(30) Kéri, A.; Dahn, R.; Krack, M.; Churakov, S. V. Combined XAFS spectroscopy and ab initio study on the characterization of iron incorporation by montmorillonite. *Environ. Sci. Technol.* **2017**, *51*, 10585−10594.
(31) Kèri, A.; Dähn, R.; Krack, M.; Churakov, S. V. Characterization of structural iron in smectites-An ab initio based X-ray spectroscopy study. *Environ. Sci. Technol.* **2019**, *53*, 6877−6886.
(32) Cametti, G.; Scheinost, A. C.; Giordani, M.; Churakov, S. V. Framework modifications and dehydration path of a Ag^{+}-modified zeolite with STI framework type. *J. Phys. Chem. C* **2019**, *123*, 13651−13663.
(33) Cametti, G.; Scheinost, A. C.; Churakov, S. V. Structural modifications and thermal stability of Cd2+-exchanged stellerite, a zeolite with STI framework type. *J. Phys. Chem. C* **2019**, *123*, 25236−25245.
(34) Funke, H.; Scheinost, A. C.; Chukalina, M. Wavelet analysis of extended X-ray absorption fine structure data. *Phys. Rev. B* **2005**, *71*, No. 094110.
(35) Gellens, L. R.; Mortier, W. J. Uytterhoeven. On the nature of the charged silver clusters in zeolites of type A, X, Y. *Zeolites* **1981**, *1*, 11−18.
(36) Sun, T.; Seff, K. Silver clusters and chemistry in zeolites. *Chem. Rev.* **1994**, *94*, 857−870.
(37) Calzaferri, G.; Forss, L. An Ag-atom in the 6-6 subunit of a zeolite: Model calculations. *Helv. Chim. Acta* **1986**, *69*, 873−880.
(38) Fiddy, S. G.; Bogdanchikova, N. E.; Petranovskii, V. P.; Ogden, J. S.; Avalos-Borja, M. EXAFS and Optical Spectroscopy Characterisation of Silver within Zeolite Matrices. In *Studies in Surface Science and Catalysis*; Elsevier, 2002; Vol. *142*, pp 1939−1946.
(39) Lee, S. H.; Kim, Y.; Seff, K. Weak Ag^{+}−Ag^{+} bonding in zeolite X. Crystal structures of $Ag_{92}Si_{100}Al_{92}O_{384}$ hydrated and fully dehydrated in flowing oxygen. *Microporous Mesoporous Mater.* **2000**, *41*, 49−59.
(40) Kim, Y.; Seff, K. Structure of a very small piece of silver metal. The octahedral Ag_6 molecule. Two crystal structures of partially decomposed vacuum- dehydrated fully Ag^{+}-exchanged zeolite A. *J. Am. Chem. Soc.* **1977**, *99*, 7055−7057.
(41) Kim, S. Y.; Kim, Y.; Seff, K. Two crystal structures of fully dehydrated, fully Ag+-exchanged zeolite X. Dehydration in oxygen prevents Ag^{+} reduction. Without oxygen, Ag_8^{n+} (T_d) and *cyclo*-Ag_4^{m+} (near S_4) form. *J. Phys. Chem. B* **2003**, *107*, 6938−6945.
(42) De Cremer, G.; Coutino-Gonzales, E.; Roeffaers, M. B. J.; Moens, B.; Ollevier, J.; Van der Auweraer, M.; Schoonheydt, R.; Jacobs, P. A.; De Schryver, F. C.; Hofkens, J.; De Vos, D. E.; Sels, B. F.; Vosch, T. Characterization of fluorescence in heat-treated silver-exchanged zeolites. *J. Am. Chem. Soc.* **2009**, *131*, 3049−3056.
(43) Kim, Y.; Seff, K. The hexasilver molecule stabilized by coordination to six silver ions. The structure of (Ag+)6(Ag)6. The crystal structure of an ethylene sorption complex of partially decomposed fully Ag+-exchanged zeolite A. *J. Am. Chem. Soc.* **1978**, *100*, 175−180.
(44) Rai, M.; Yadav, A.; Gade, A. Silver nanoparticles as a new generation of antimicrobials. *Biotechnol. Adv.* **2009**, *27*, 76−83.
(45) Granger, P.; Parvulescu, V. I. Catalytic NO_x abatement systems for mobile sources: form three-way to lean burn after-treatment technologies. *Chem. Rev.* **2011**, *111*, 3155−3207.
(46) Pan, H.; Su, Q.; Chen, J.; Ye, Q.; Liu, Y.; Shi, Y. Promotion of Ag/H-BEA by Mn for lean NO reduction with propane at low temperature. *Environ. Sci. Technol.* **2009**, *43*, 9348−9353.
(47) Matsuoka, M.; Anpo, M. Photoluminescence properties and photocatalytic reactivities of Cu+/zeolite and Ag+/zeolite catalysts prepared by the ion-exchange method. *Curr. Opin. Solid State Mater. Sci.* **2003**, *7*, 451−459.

https://dx.doi.org/10.1021/acsomega.0c04455
ACS Omega 2020, 5, 31774−31783